Experimental and numerical study of turbulence effect on aerodynamic performance of a small-scale vertical axis wind turbine

David Wafula Wekesa [a,b,*], Cong Wang [a], Yingjie Wei [a], Weidong Zhu [a,c]

[a] Department of Aerospace Engineering and Mechanics, School of Astronautics, Harbin Institute of Technology, Harbin City, PR China
[b] Department of Physics, Jomo Kenyatta University of Agriculture & Technology, Nairobi City, Kenya
[c] Department of Mechanical Engineering, University of Maryland, Baltimore County, Baltimore, United States

ARTICLE INFO

ABSTRACT

The suitability of vertical axis wind turbines (VAWTs) in harnessing energy within a complex wind environment has increased their renewed interest. However, there still exists a huge knowledge gap about the aerodynamic performance of VAWTs operating in a turbulent flow regime. In this paper, an experimental method is presented for a deeper understanding of unsteady rotor aerodynamics under turbulent flow operating conditions. To carry out the investigation, we developed and tested a small-scale Savonius turbine in a wind tunnel. A systematic analysis of torque and power coefficients, including their variations at uniform flow, was also presented to predict the power performance. A mechanism to generate a turbulent flow was then created to analyze the effect of induced turbulence intensity on the aerodynamics and performance of the VAWT. Results revealed that the turbulence of the inflow impacted fluctuating aerodynamic loads on the turbine blade and, ultimately, its aerodynamic performance. In addition, simulations using a CFD code were performed to compare numerical data with experimental measurements. This analysis shows the effect of turbulence intensity on performance of small wind turbines, and the aerodynamics that causes the behavior.

© 2016 Elsevier Ltd. All rights reserved.

1. Introduction

Turbulence is a complex process and can have a significant impact on the power output of wind turbines. This is particularly crucial for small wind turbines, which in practice are typically installed near buildings, trees, and other obstacles (McIntosh et al., 2008; Mcintosh, 2009; Scheurich, 2011). The vertical axis wind rotors have potential advantages under such conditions due to their ability to accept wind from any direction without yawing, low sound emission due to relatively lower tip speed ratios, increased performance in unsteady and skewed flows, ease of maintenance and low manufacturing cost, as well as potential operational safety during gust conditions (Edwards et al., 2012; Danao et al., 2013, 2014; Wekesa et al., 2014b, 2015, and references therein). Two types of VAWTs are mainly used, Savonius and Darrieus wind rotors (Wekesa et al., 2014b, 2015; Islam et al., 2008). The Savonius rotors are the simplest and cheapest designs of wind turbine rotors and have the capability to self-start at low wind speeds from any direction. Various experimental studies have been carried out to improve the aerodynamic performance of Savonius wind turbines (Mahmoud et al., 2012; Saha and Rajkumar, 2006; Jeon et al., 2015; Nasef et al., 2013; Tesch et al., 2015; Bhuyan and Biswas, 2014; Torresi et al., 2014; Gupta et al., 2008, and references therein). The studies revealed that Savonius wind turbines are an interesting technological alternative to conventional wind turbines.

There is relatively scarce literature that has attempted to characterize the effect of wind turbulence on the turbine's performance. The current power curve representations do not account for the impact of turbulence on small wind turbine energy production (Lubitz, 2014; He et al., 2013; Seguro and Lambert, 2000; Sparks and Huang, 2001). The common approach to report the turbine power curves is to determine output power as statistical averages of power measurements binned by wind speed, whereby the variance of the data is lost (Lubitz, 2014; Ahmadi-Baloutaki et al., 2015; Rogers et al., 2005; Fyrippis et al., 2010; Cao et al., 2009). This approach does not capture the effect of free-stream turbulence, thus creating an immediate need to address the influence of turbulence intensity and providing useful information in the context of wind turbine power curve.

A few studies that have attempted to characterize the effect of wind turbulence on wind turbines indicate that turbulence effect on wind turbine performance installed in urban environment is

subjected to intensity of the turbulence as well as the size of turbulence scales (Lubitz, 2014; Ahmadi-Baloutaki et al., 2015; Sunderland et al., 2015; Pagnini et al., 2015; Maldonado et al., 2015; Kooiman and Tullis, 2012; Turk and Emeis, 2010; Mycek et al., 2014; Emejeamara et al., 2015; Bertenyi et al., 2010, and references therein). Unlike typical atmospheric performance testing works, the output data from studies in Lubitz (2014), Sunderland et al. (2015), Pagnini et al. (2015), Kooiman and Tullis (2012), and Turk and Emeis (2010) were split into smaller segments and the variance of the data was used to determine the turbulence intensity of each segment. Wind turbulence levels lower than 14% resulted into increased power output, while inconsistent trend was reported for higher turbulence levels. The authors (Lubitz, 2014) asserted that the turbine rotor energy production was altered by ambient turbulent levels, although the impact varied at different wind speeds. However, all tests were performed in an open atmospheric environment; hence there was no control on the level of free-stream turbulence.

The studies in Pagnini et al. (2015), Maldonado et al. (2015), Mycek et al. (2014), Emejeamara et al. (2015), and Mikkelsen (2013) have pointed out the significant role of the ambient turbulence intensity rate on the aerodynamic performance of wind turbines. Pagnini et al. (2015) employed two small-size wind turbines, with horizontal (HAWT) and vertical (VAWT) axis to analyze power curves in turbulent urban environment. From Pagnini et al. (2015), the VAWT became more efficient and started producing more power than HAWT quite often, especially at higher turbulence conditions. A similar study by Maldonado et al. (2015) experimentally determined the role of free-stream turbulence with large integral scale on the aerodynamic performance of a wind turbine blade. A significant increase in the lift-to-drag ratio for most angles of attack was predicted at high levels of turbulence intensity. However, although a turbulent free-stream may increase turbine power, the blades must be designed to withstand prevalent larger mean and fluctuating aerodynamic loads and thus cyclic stresses due to turbulence (Maldonado et al., 2015). In addition, Mycek et al. (2014) run experimental trials at two turbulent intensities, namely 3% and 15%, from which the wake remains pronounced. This corresponded to almost 20% velocity deficit and more than three times the upstream ambient turbulence intensity at lower turbulence intensity. While, at a higher turbulence intensity, the wake dissipated much faster.

There is no clear consensus on the effect of free-stream turbulence on wind turbine's aerodynamic performance induced by turbulence intensity as different trends have been reported in the literature. Ahmadi-Baloutaki et al. (2015) attributed these variations to different turbulent flow type studies by different researchers, complicated by varying amounts of wind shear and unsteady winds. To further understand the systematic performance of small wind turbines under controlled turbulent flow with steady and uniform wind conditions, Ahmadi-Baloutaki et al. (2015) attempted to investigate the influence of free-stream turbulence intensity on the aerodynamic performance of a Darrieus-type VAWT. A marginal increase in turbine power coefficient was predicted by increasing the turbulence intensity beyond 5% in the grid generated turbulent flows. In addition, the introduction of the external free-stream turbulence improved the self-starting capability of the vertical axis wind turbine. However, the turbine performance curves were limited to lower tip speed ratios ($\lambda < 1$) (Ahmadi-Baloutaki et al., 2015). Hence, for complete interpretation of the effect of free-stream turbulence on the wind turbine performance, there is need for extending the performance curves to tip speed ratios greater than one. In addition, generation of performance curves at greater tip speed ratios in turbulent flows still remains a challenge in research owing to limitations in wind tunnel experiments and safety considerations.

Therefore, the present study capitalizes on such aspects and employs an experimental method to investigate the influence of turbulence intensity on aerodynamic performance of a small-scale Savonius-type VAWT. A turbulence-generating mechanism has been used to generate the simplest form of turbulence. In addition, the general wind turbine model setup is discussed, and simulations using a CFD code are performed for comparison between experimental measurements and numerical data.

2. Experimental description

This section aims at giving a detailed description of the experimental setup, instrumentation, and measurement procedures used for the experiments.

2.1. The wind tunnel facility

The experiment of the VAWT model was performed in advanced wind tunnel and wave flume joint laboratory situated at Harbin Institute of Technology (HIT). The wind tunnel is a closed-loop circuit, which consists of double test sections: the small test section and the large test section. The small test section is 4.0 m (width) × 3.0 m (height) with a length of 25.0 m, and the large section is 6.0 m (width) × 3.6 m (height) with a length of 50.0 m. The turbine model tests in this study were performed in the small test section with optically transparent walls, with a background turbulence intensity of less than 0.46% at the end of the test section under normal operation. The flow with $I < 0.46\%$ in the present study is deemed 'no turbulence' or uniform flow. In addition, the wind tunnel has a characteristic of good flow field performance with test flow field inhomogeneity and mean flow angle of less than 1% and 0.5°, respectively. The maximum achievable velocities are 50 m/s and 30 m/s for the small and large empty working test sections, respectively. A wave trough is located under the large test section and separated by moving floors. The VAWT model is mounted on a fixed circular turntable 3.6 m in diameter at the center of the test section, 6 m downstream distance along the test section length; a schematic diagram of the facility is shown in Fig. 1.

Additional levels of free-stream turbulence ($9 \geq I \leq 14\%$) used in the experiments to simulate turbulent inflow conditions were generated using an active turbulence-generating wedge mechanism located at the end of the test section inlet. The turbulence levels were chosen to match the unsteady urban wind environment which is a representative of the prevailing wind characteristics of a target site in Kenya following a previous study by the authors in Wekesa et al. (2015). The turbulence-generating wedges were placed 16 m from the VAWT model along the 19 m upstream distance of the wind tunnel test section length. The active wedge mechanism consists of seven vertical elliptical shafts 0.5 m apart firmly fixed and spanning the height and width of the wind tunnel test section. Figs. 2(a) and (b), respectively, show a photograph of the active turbulence-generating mechanism and the VAWT model fixed on the test stand in a wind tunnel test section.

The flow field surrounding VAWTs is asymmetric, periodic, unsteady, separated and highly turbulent (Ahmadi-Baloutaki et al., 2015). Although wind tunnel tests provide benefit for controlled flow conditions, further sources of error due to the effect of blockage are introduced during the process. Therefore, characteristics of the flow would be altered to some extent if an obstruction is placed within the wind tunnel. The blockage ratio, BR, is defined as the ratio of the cross-sectional area of the rotor model to the maximum wind tunnel projected test section area: BR=rotor frontal area/test section area (Jeon et al., 2015). The frontal area of the present VAWT rotor as it spins is 0.49 m², resulting into a
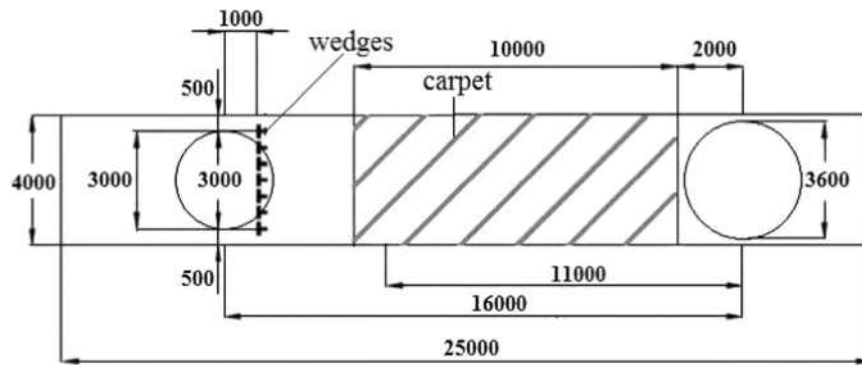
Fig. 1. Wind tunnel facility of the Harbin Institute of Technology (dimensions in mm).
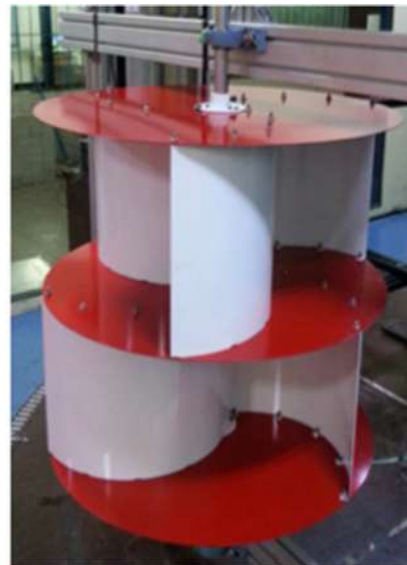

(a) Elliptic wedge generators   (b) VAWT test model for turbulent flow

Fig. 2. Turbulence-generating mechanism and the VAWT model in a wind tunnel.


(a)   (b)

Fig. 3. CAD turbine rotor model assembly (a) and wind tunnel test rotor model (b).

blockage ratio of 4.1% in the present study test. Such a small blockage area ratio has a negligible effect on the flow, and that for blockage ratios less than 6%, no correction is needed for output results (Howell et al., 2010). Therefore, it was not necessary to consider the effects of blockage in the present study as absolute performance levels were not intended; instead only relative performance levels were intended to address fundamental understanding of turbulence flow effects on the aerodynamic performance of small vertical axis wind rotors. The wind tunnel was operated at fixed mean free-stream velocities upstream of the
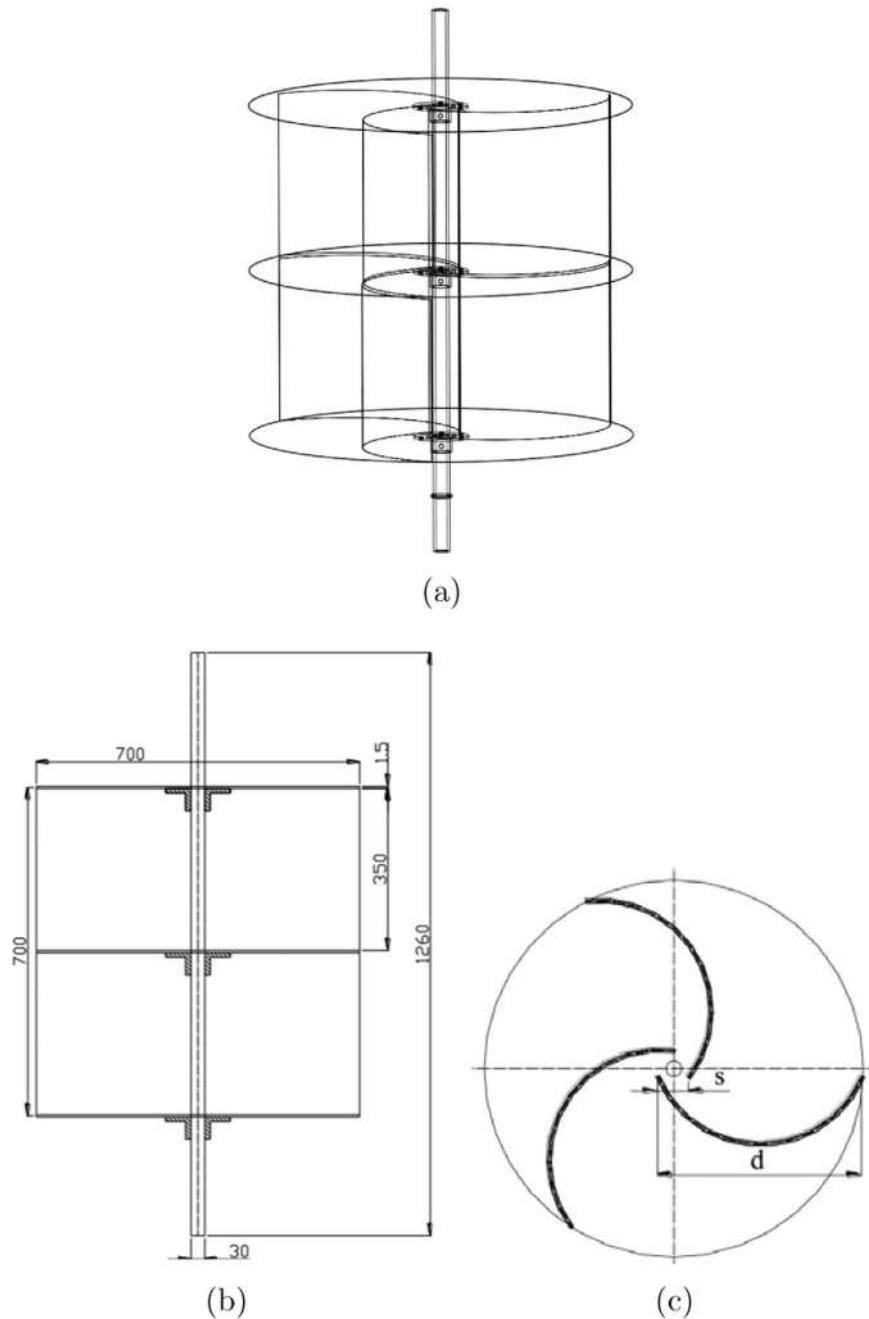
Fig. 4. Overview of the modelled Savonius rotor design (dimensions in mm). (a) Isometric view of the rotor. (b) Side view of the rotor. (c) Top view of the rotor.

Table 1
Main geometric features of the three-bladed rotor model.

Parameters	Design dimension	Unit
Blade material	Galvanized iron sheets	
Rotor stages	Two stages	
No. of blades per rotor stage	3	
Total no. of Savonius blades	6	
Height (H)	0.70	m
Rotor diameter (D)	0.70	m
Blade and end plate thickness (t_i)	0.001	m
Overlap ratio β	0.15	
Aspect ratio A_R	1.0	
Wind speed condition	4–11	m/s

blade at U_∞ = 11, 8, 7, 6, and 4 m/s with turbulence intensity within the range of 9–14%. In addition, similar tests were repeated under a uniform flow across the wind velocities without the turbulence-generating mechanism for comparison.

2.2. Rotor model

The experiment utilized a Savonius-type VAWT with three blades as shown in Fig. 3. Before manufacture, a CAD model was used to carry out the design (Fig. 3) to reduce the likelihood of anticipated problems during the design. The VAWT rotor geometry has a central shaft with a diameter of 0.030 m running through the top and bottom walls of the test section.
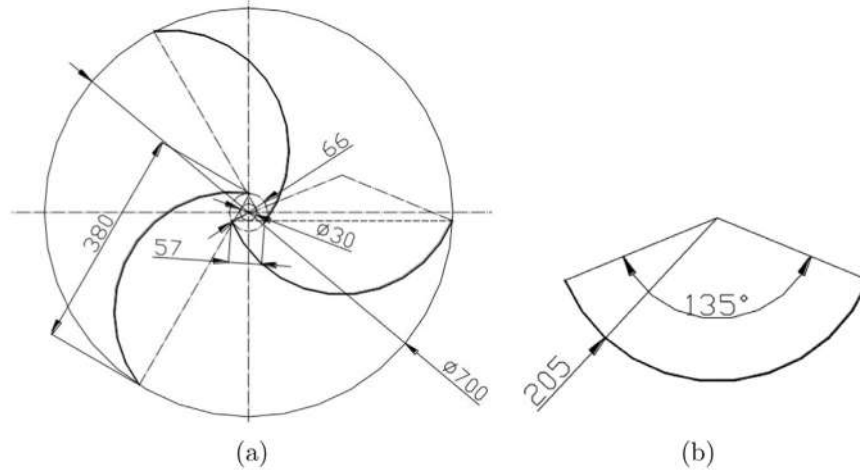
Fig. 5. Developed Savonius blade profile (dimensions in mm). (a) Top view. (b) Top view for single blade.

In the present study, a modified three-bladed double-stage Savonius rotor is considered for the experimental investigation as represented in Fig. 4. The double-stage rotor is adapted in the present study following its higher efficiency than single-stage rotor as asserted in the literature (Mahmoud et al., 2012; Akwa et al., 2012). The dimensions of the turbine rotor parts selected are as shown in Table 1.

The modified blade with an overlap ratio (overlap distance: blade diameter) $\beta = 0.15$, aspect ratio (rotor height: rotor diameter) $A_R = 1.0$, and end plate parameter value of 1.0 aims to improve greatly the rotor aerodynamics (lift and drag) and performance (power and torque coefficients) over the conventional Savonius wind turbines. The rotor blades are fabricated from galvanized iron sheets of thickness $t_i = 1.0$ mm constructed in the form of cylindrical halves with semi-circular cross sections.

Fig. 5 shows the dimensions of the developed Savonius blade profile consisting of several individual arcs. The end plates have been used at both the tops and at the bottoms of the double-stage Savonius turbine model to improve its performance. This is aimed at improving pressure difference between the convex and concave surfaces of the Savonius rotor blades (Roy and Saha, 2015).

2.3. Instrumentation and measurement procedures

The Savonius rotor model was fully operational and the power extracted from the wind could be measured directly using torque transducer (JN338A rotary torque sensor) with a measurement scale ranging from 0 N m to 2 N m having an acceptable precision of 0.01 N m. Rotational speeds of the turbine rotor were also obtained from the torque transducer and the maximum rotational speed of the transducer was 3000 rpm. The dimensionless performance parameters commonly used in the aerodynamics of wind turbines are often measured in terms of torque coefficient C_m and power coefficient C_P, which are usually determined as a function of tip speed ratio λ. The definitions are as follows (Wekesa et al., 2014b, 2015):

$$C_m = \frac{T}{\frac{1}{2}\rho A R_{rotor} U_\infty^2},$$
(1)

$$C_P = \frac{P_{blade}}{P_{wind}} = \frac{T\omega}{\frac{1}{2}\rho A U_\infty^3} = \frac{T}{\frac{1}{2}\rho A U_\infty^2 R_{rotor}} \frac{\omega R_{rotor}}{U_\infty} = C_m \times \lambda,$$
(2)

$$\lambda = \frac{\omega R_{rotor}}{U_\infty} = \frac{2\pi N}{60} \frac{R_{rotor}}{U_\infty},$$
(3)

where T is the turbine blade torque, ρ is the air density, U_∞ is the free-stream wind speed, $A = H \times D = 0.7$ m $\times$ 0.7 m is the turbine swept area where D is the diameter of the rotor and H is the rotor's height, R_{rotor} is the rotor radius, P_{blade} is the power produced by the turbine blades, P_{wind} is the power available in the wind, ω is the rotational speed, and N is the rotational speed per minute (rpm). However, for the transient flow, which is a typical for the Savonius rotor operation, the total energy of the wind within the time interval Δt as opposed to the instantaneous power should be considered. As a result the definition in Eq. (2) takes the form (Tesch et al., 2015):

$$C_P = \frac{\omega \int_t^{t+\Delta t} T(t)\mathrm{d}t}{\frac{1}{2}\rho A U_\infty^3} = \frac{\omega\bar{T}}{\frac{1}{2}\rho A U_\infty^3},$$
(4)

where Δt stands for the time of interest, for instance time in one full rotor rotation. Assuming that the time step of transient flow CFD calculations is constant, the integral in Eq. (4) can be approximated as $\bar{T} = n^{-1}\sum_{i=1}^{n} T_i$ where $\bar{T}$ is the arithmetic average (Tesch et al., 2015).

The free-stream reference wind velocity in the working section was measured using a Pitot-static pressure probe. A mechanical ball bearing disc brake was developed and employed in maintaining reasonably constant average rpm by varying the load applied to the VAWT. Thus the behavior of the power coefficient, C_P, could be observed at different rpm. The experimental setup is shown schematically in Fig. 6.

Two bearing units were used to mount the turbine rotor assembly on the shaft, which was fixed between the top and bottom of the wind tunnel test section to allow free rotation of the rotor shaft. A third bearing unit was adapted to support and firmly hold the ball bearing disc brake and the shaft on the frame. From Fig. 7, the top and bottom ends of the model were erected such that they were far away from the support frame. This was to minimize the airflow disturbance during the turbine rotation. A pillow block bearing at the bottom supported the weight of the radial load of the shaft by acting as a thrust bearing.

All components of the rotor geometry were attached such that they could be assembled or adjusted with ease. To enable accurate measurements, the aerodynamic forces were measured as large as possible, and the system resistances as minimal as possible. In the present experimental study, very small values of rotor torque are measured. An easy way and solution around this was to set a
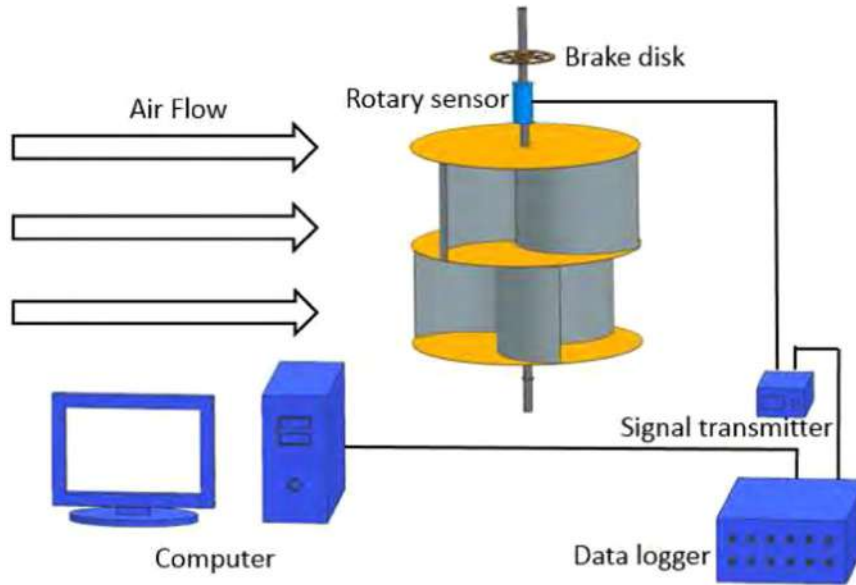
Fig. 6. Savonius drag-based VAWT measurement apparatus.

sensor resolution as low as possible at 0.01 N m to detect small values of torque. In addition, for tests at higher wind speeds, the application of the ball bearing disc brake was required because of positive rotor torque which caused the VAWT models to cut-in without coming to rest.

Fig. 8 shows the working components of the test stand with a rotary sensor for measuring torque and rotational speed. Observe that (Fig. 8), two spider shaft coupling were connected at both ends of the sensor. The rotary sensor with data logger was connected to the rotor shaft of the VAWT model to measure the rotational speed (rpm), torque, and power generation. The logging frequency was set such that it was at least 30 times faster than the rotational frequency of the VAWT. In the current study, the data logging frequency of 1024 Hz was set such that the torque ripples in one rotation could be seen. The signals (torque and rpm) from the torque sensor were read and appropriately scaled by a signal transmitter with the computer data acquisition (DAQ) card connected to a desktop running computer (Fig. 6).

The specified wind speed for all our tests from the wind tunnel ranged from 4 m/s to 11 m/s based on the assumption that small wind turbines, like Savonius make measurements more difficult. This is because high wind speeds exert high pressure on the rotor blades that may cause the turbine to exceed its design limits, thus posing danger due to uncontrolled angular motion. In addition, the wind turbine in the present study is meant for urban wind condition applications and, therefore, wind speeds of 11 m/s or higher would be rarely encountered. For tests where control of the VAWT rpm is required, the spider shaft coupling connects the disc brake shaft such that the rotor rpm can be set and held at a constant value.

3. Wind velocity and turbulence intensity profiles

The wind velocity and turbulence intensity profiles were obtained by putting up masts with anemometers at the wind tunnel test section and the wind speed measured over time in the absence of the turbine. Due to time and huge costs involved, mathematical models are commonly used to estimate vertical wind shear for turbines. The two mathematical models widely used to approximate the wind velocity profile in the atmospheric boundary layer (ABL) are the log-law and the power law. The equation

known as the logarithmic wind profile is defined as (Mikkelsen, 2013):

$$\bar{u}(z) = \frac{u^*}{\kappa}\ln\left(\frac{z}{z_o}\right),\tag{5}$$

where $\bar{u}$ is the mean wind speed, z is the elevation above the ground, u^* is the shear velocity (m/s), κ is Von Karman's constant ($\kappa = 0.40$), and z_o is the surface roughness length (m). According to Eq. (5), wind velocity increases logarithmically with increasing height within the boundary layer depending on the surface roughness and atmospheric stability. However, for neutral stability conditions (adiabatic conditions), the stability term drops out. As a result, the power law is generally used as a substitute for log wind profile to determine the velocity profile in the absence of surface roughness and atmospheric stability information. The basic form of the power law is (Mikkelsen, 2013):

$$\frac{u(z)}{u_{ref}} = \left(\frac{z}{z_{ref}}\right)^\alpha,\tag{6}$$

where $u(z)$ is the wind speed at height z, u_{ref} is the reference wind speed at the reference height z_{ref}, while α is the power law exponent which depends on the surface roughness and the atmospheric stability.

The power law is widely used due to its simplicity, and it seems to give a better fit to most of the data over a greater height range and for higher wind conditions, compared with the log-law (Mikkelsen, 2013). Turbulence in the ABL causes fluctuations in both wind speed and direction, which are key factors in wind turbine siting and blade design for efficient power production. A pitot-static pressure probe was placed in an empty tunnel test section, 0.4 m high, which is the position of the center of the VAWT rotor to find the real reference wind speed. Five measuring positions at interval of 0.2 m were taken with one position below and four positions above the reference level. The turbulence intensity at the wind tunnel test section in the absence of turbine was determined by

$$I(\%) = \frac{u_{rms}}{\bar{u}} \times 100,\tag{7}$$

where $\bar{u}$ is the time average of the streamwise velocity signal and u_{rms} is the root-mean square of the velocity fluctuations in the
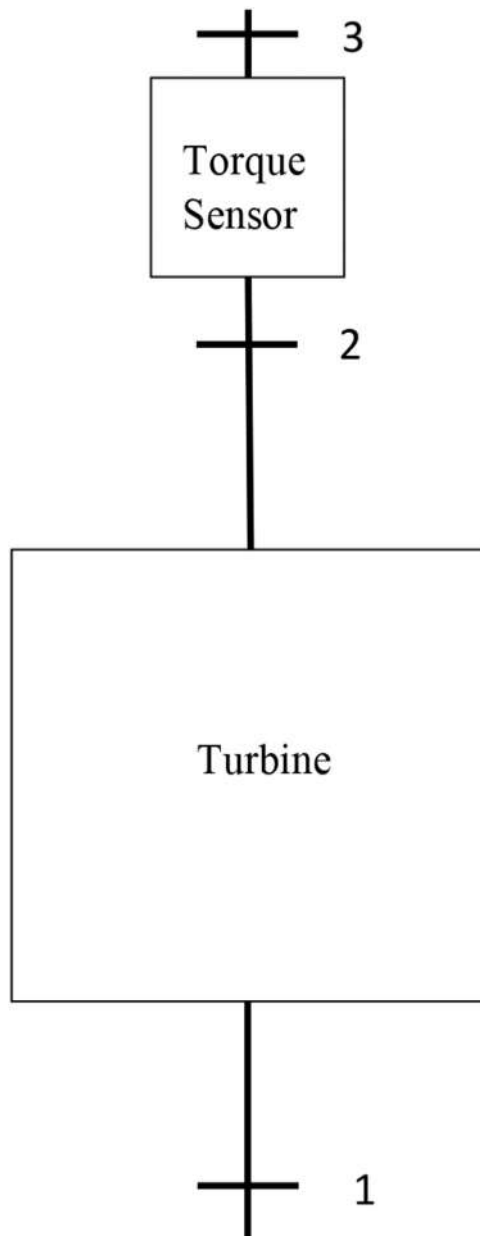
Fig. 7. Bearing schematic: 1. bottom bearing, 2. middle bearing, and 3. top bearing.
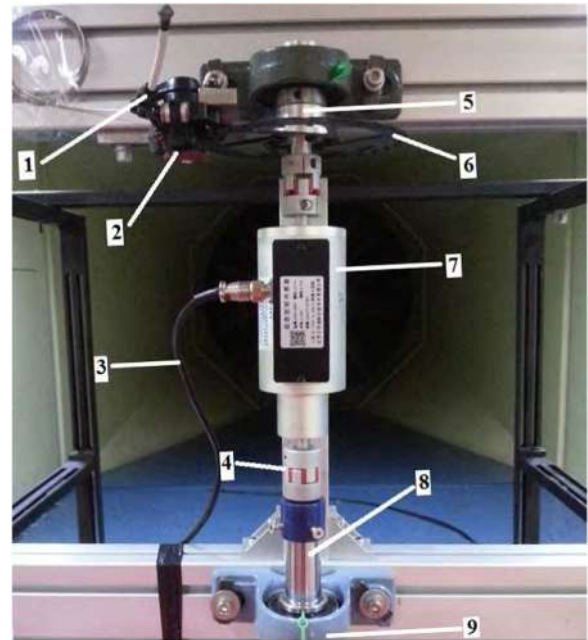

Fig. 8. Test stand working components: 1. brake caliper, 2. adjusting knob, 3. transmitter signal interface, 4. spider shaft coupling, 5. brake disc mount, 6. brake disc, 7. rotary torque sensor, 8. shaft, and 9. pillow block ball bearing.

streamwise direction calculated from

$$u_{rms} = \sqrt{\frac{1}{n-1} \sum_{i=1}^{n} \left(u_i - \overline{u} \right)^2}, \tag{8}$$

where n is the sample number in velocity signals and u_i is the streamwise velocity component for individual velocity signal (Mikkelsen, 2013). The turbulence intensity depends on the roughness of the earth's surface, the height above the ground, topological features and the thermal behavior of the atmosphere. Fig. 9 shows the wind velocity profile and the turbulence intensity of the wind tunnel test section for the present study. From Fig. 9 (a), the wind velocity test profile shows a close match to the theoretical power law profile with an exponent value of 0.1429. The exponent value of 0.1429 has been chosen following previous work by the authors in Wekesa et al. (2014a,b, 2015) as a good representative of the prevailing wind conditions. Observe in Fig. 9 (b) that the turbulence intensity is within the range of 9–14%.

4. Experimental results and discussion

The uniform and turbulent flows tests detailed in Section 2 are compared to investigate the aerodynamic performance of the VAWT. The experimental results for power and torque coefficients are as shown in Figs. 10 and 11, respectively. It can be observed from the uniform flow C_P distribution in Fig. 10(a) that the power curves increase with increase in free-stream wind velocity across the entire λ range under study. While, from Fig. 10(b) for turbulent flow case, both decrease and increase in power performances are revealed at high and low wind speeds, respectively.

As can be seen in Fig. 10(b), it is clear that for a turbulent flow condition, on the one hand, the power coefficient distribution increases drastically for low wind speeds at 4 m/s, 6 m/s, and 7 m/s contrary to the uniform flow (Fig. 10(a)). On the other hand, the power coefficient distribution decreases for high wind speeds at 8 m/s and 11 m/s. The increase in the power coefficient in the turbulent flow case is very small at 7 m/s compared to wind speeds at 6 m/s and 4 m/s.

Another improvement in the turbine aerodynamic operation is the reduction of the self-starting speed in the presence of the wedge turbulence mechanism. As evidenced in Figs. 10(a) and (b), the turbine self-started at tip speed ratio of 0.17 for uniform flow at wind velocities of 4 m/s and 11 m/s, while the self-starting occurred earlier at tip speed ratios of 0.16 and 0.11 for turbulent flow at wind velocities of 4 m/s and 11 m/s, respectively. Observe in Fig. 10 that, the optimal tip speed ratio is shifted to the right across the wind speeds for the turbulent flow case. This could be attributed to the change in the flow around the rotor blade such that stall effects were more severe at low tip speed ratio characterized by a wide large angle of attack as compared to the uniform inflow case.

The significant improvement in turbine's aerodynamic performance at low wind speeds (within the range of 4–7 m/s) when the wind turbine is subjected to turbulent flow can also be detected in Fig. 11(b) by noticing the substantial increase in torque coefficient in the wedge turbulent flow compared to the uniform flow case. Observe in Fig. 11(a) that the torque coefficient takes on maximum
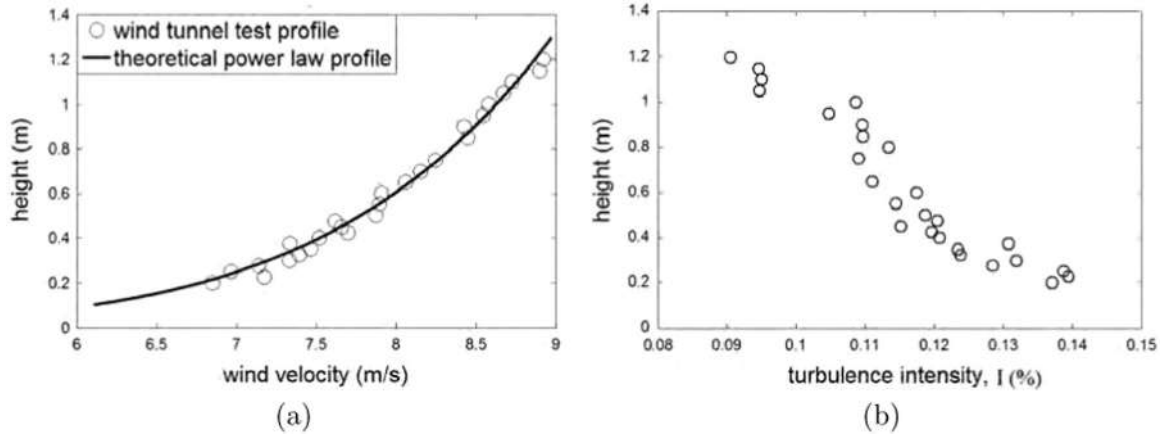
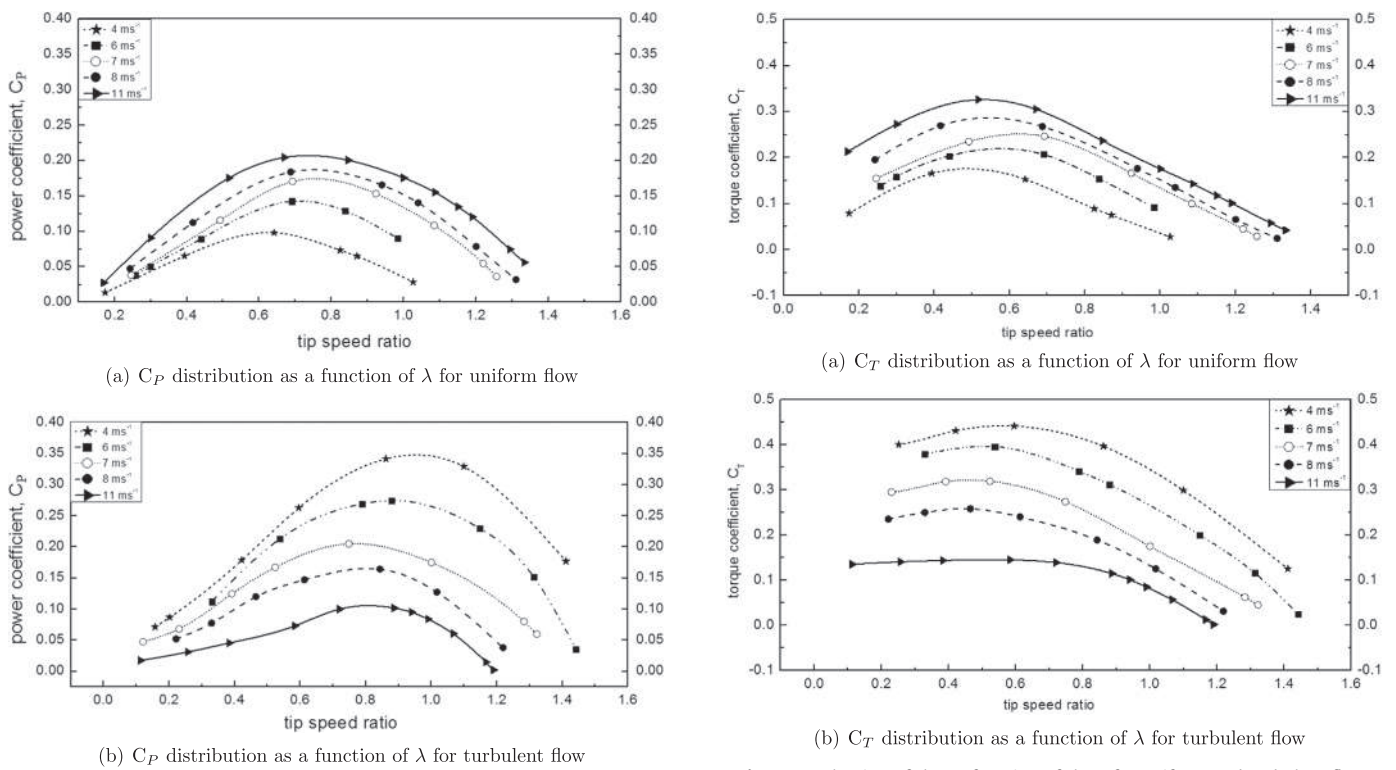Fig. 9. (a) Wind velocity profile of the test section. (b) Turbulence intensity.

(a) C_P distribution as a function of λ for uniform flow

(b) C_P distribution as a function of λ for turbulent flow

Fig. 10. Evaluation of the C_P function of the λ for uniform and turbulent flow.

(a) C_T distribution as a function of λ for uniform flow

(b) C_T distribution as a function of λ for turbulent flow

Fig. 11. Evaluation of the C_T function of the λ for uniform and turbulent flow.

peaks of 0.34 and 0.27 obtainable at wind velocities of 11 m/s and 8 m/s, respectively. However, for turbulent flow case in Fig. 11(b), the torque coefficient peaks drops to 0.16 and 0.26 at 11 m/s and 8 m/s, respectively. While, the torque coefficient peaks significantly increase from 0.21 and 0.17 for uniform flow case to 0.40 and 0.44 for turbulent flow case at 6 m/s and 4 m/s, respectively.

As can be seen in Fig. 10, the uniform flow case (Fig. 10(a)) reveals reduced power coefficient compared to turbulent flow case (Fig. 10(b)) for wind speeds at 7 m/s, 6 m/s, and 4 m/s. Implying that, this is roughly the operating range above cut-in and below the beginning of turbine's furling speed. Above 7 m/s, at wind speeds of 8 m/s and 11 m/s, a drastic reduction in power generation is evident for the turbulent flow, suggesting an earlier furling than would otherwise occur in uniform flow. In addition, the reduction of power generation exhibited above mean wind speeds of 7 m/s for turbulent flow case shows that the turbine experiences furling at wind speeds above 7 m/s for the present wind condition. The detrimental effects of turbulence are most pronounced at

wind speeds approaching the furling, thus reducing power generation of the wind turbine. Otherwise, at mean wind speeds below turbine's furling speed, more turbulent winds are seen to generate greater power than less turbulent winds. This could be attributable to the cubic variation of power with wind speed.

The improved blade aerodynamic efficiency for the turbulent flow case was attributed to increased ratio in aerodynamic forces, delaying the dynamic stall, and postponing the flow separation over the blade surfaces (Aslam Bhutta et al., 2012; Paraschivoiu, 2002). Furthermore, stall effects were more severe at low tip speed ratios where turbine rotor blades experienced a wide range of angle of attack mostly located in the stall region of the blade (Aslam Bhutta et al., 2012; Paraschivoiu, 2002).

Maldonado et al. (2015) attributed the increased blade aerodynamic efficiency as a result of turbulence intensity to flow re-attachment at high angle of attack. The large velocity fluctuations associated with free-stream turbulence intensity interacted with the turbulence layer over the wind turbine blade, contributing to

kinetic energy that dissipated in the smaller scales of the boundary layer (Maldonado et al., 2015). This caused delay of flow separation that was observed in high angle of attack.

The current study optimal tip speed ratios are in the low range region where positive effects of turbulence intensity are more effective. Generally, at low wind speeds, turbulence appeared to increase energy production for the current turbine. In contrast, at wind speeds near the turbine furling speed, turbulent flows results to decrease in power performance, attributable to the turbulent gusts initiating furling events. It is noteworthy that in order to create more accurate power production estimates, turbine manufacturers could provide power curves for different turbulence levels combined with site observations.

5. CFD simulations

This section provides simulations using a CFD code performed to compare numerical data with experimental measurements (as outlined in Section 2).

5.1. Computational domain

A CFD computational domain of rectangular shape with a length of 36 rotor diameters has been chosen as shown in Fig. 12, having the same wind tunnel external sizes. A relative width (4.0 m) and height (3.0 m) of the test section was chosen such that it matches the experimental wind tunnel dimensions detailed in Section 2 with a blockage area of 4.1%. As can be seen in Fig. 12, the computational domain consists of two mesh zones: the inner rotor sub-grid zone where the rotating motion is defined by the rotating reference frame technique in order to capture the generated torque and the wind tunnel sub-grid static zone where fixed motion is applied. A cylindrical interface was created between the stationary and rotating zones. The interface of the two mesh zone boundaries slide against each other with no excessive overlap to minimize numerical diffusion, and have approximately the same characteristic cell size in order to obtain faster convergence.

The inner rotor sub-grid zone is composed of the three-bladed double stage Savonius VAWT rotor geometry rotating at a common angular velocity. The 3D CFD model was used to represent the wind tunnel section to reveal and predict the aerodynamic performance and the flow physics around the VAWT rotor. The grid was generated using the software ANSYS® ICEM CFD as a preprocessor for mesh generation. The 3D grid independence of the solutions was verified through simulations performed with grid sizes that varied from 4 to 6 million cells. In order to test the code sensitivity to the number of grid points, three unstructured meshes were adopted for the rotor sub-grid, while the wind tunnel sub-grid remained substantially the same. Having achieved mesh independence that requires the mesh to be fine enough with suitable y^+ values of less than 1 resulted in a 3D model with approximately 5 million cells. The cells expand with a growth ratio of 1.05 above the surface, giving 140 cell layers in z-direction. The minimum cell height of the first layer was set at 1/10,000 of the blade length while cells beyond the rotor were set to have a maximum cell height not to exceed 1/100 of the blade length with an overall maximum aspect ratio of 624.16. The images of the 3D inner rotor sub-grid are as given in Fig. 13. Observe in Fig. 13 (b) that the mesh on both sides of the interface (rotor sub-grid and wind tunnel sub-grid areas) has approximately the same characteristic cell size in order to obtain faster convergence.

The side boundaries are walls that model the sides of wind tunnel relative to the rotor model. Considering the relative size of the model rotor to that of the test section, the wind tunnel walls were included in the model as the effects of the wind tunnel walls were expected to be significant. The front and outlet of the domain were defined with velocity inlet and pressure outlet boundaries, respectively. The velocity inlet boundary was placed 8 rotor diameters upstream while the pressure outlet boundary was situated at 27 rotor diameters downstream with respect to rotor test section. The later considerations are necessary to provide enough space for the generation of the wake behind the rotor. Similar to the side walls, the top and bottom of the domain are defined as no-slip walls. It should be noted that the rotor test section with respect to the inlet and output boundaries is not placed in representative positions relatively to the rotor test model in the wind tunnel, but is instead further away. This avoids the potential problem of computational boundaries interacting with the flow around the turbine (Howell et al., 2010).

The turbulent intensity of 12% and turbulence viscosity ratio of 14 were applied to approximately account for the incoming flow turbulence as detailed in the wind tunnel experiment in Section 2. These conditions were selected to provide a matching turbulence intensity decay observed in the experiments. It is noteworthy that the high value of the viscosity ratio was selected not for physical accuracy of the relationship between turbulent viscosity and laminar viscosity but for the accurate predictions of the resulting turbulence intensity decay.

The computational domain is discretized using unstructured prism layer cell elements (Fig. 13(a)). Observe in Fig. 13(b) that a prism layer was used to ensure cells are normal to each other on either side of the interface. To correctly capture separation of the boundary layer, a significant effort was dedicated to adjust the mesh density for accurate flow modelling in the boundary layers. The wind flows from the inlet to the outlet boundary at a free-stream velocity of 7 m/s; and the Reynolds number based on the rotor diameter and free-stream velocity was fixed at 340,000. The free-stream velocity of 7 m/s was chosen as a representative of the real reference wind speed at the center position of the VAWT rotor in the actual experiment.
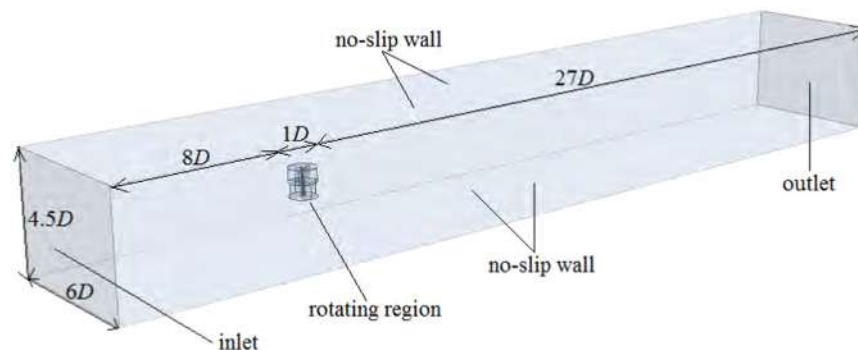

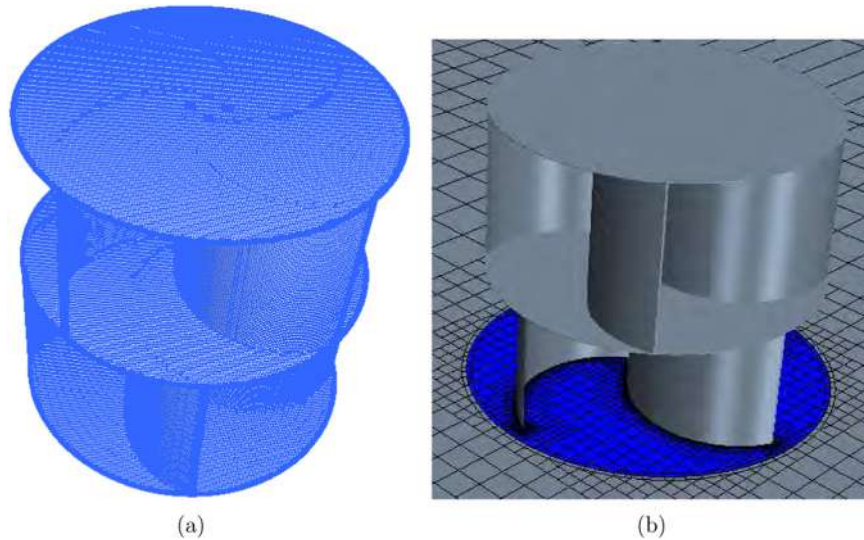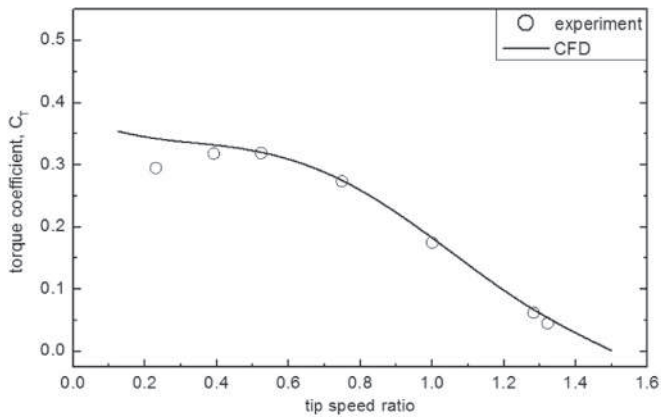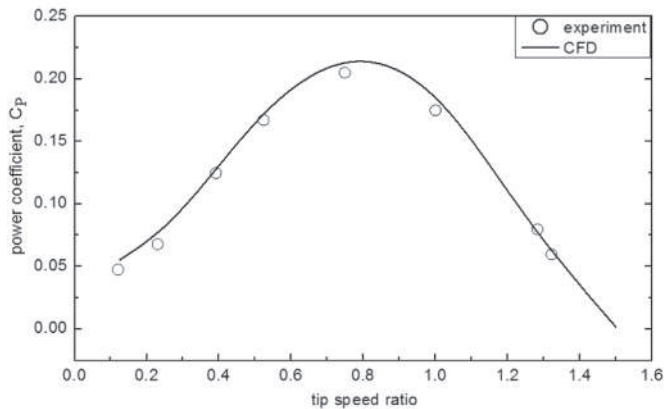**Fig. 12.** 3D overview of the wind tunnel computational domain.

Fig. 13. Overview of the inner rotor sub-grid. (a) Mesh adopted near the rotor blades. (b) Vertical rotor section along the computational domain.

(a) Torque coefficient ditribution as a function of λ at U=7 m/s.

(b) Power coefficient ditribution as a function of λ at U=7 m/s.

Fig. 14. Comparison of wind tunnel experimental results to simulations.

5.2. Numerical set-up

The simulation of flow over VAWT was studied by solving the unsteady RANS equations for the entire flow domain using commercial CFD software package ANSYS® Fluent. The incompressible, Unsteady Reynolds-Averaged Navier–Stoke's (URANS) numerical approach for the equations was used.

The Semi-Implicit Method for Pressure Linked Equations (SIMPLE) algorithm was used for coupling between pressure and velocity with a green-gauss cell based gradient evaluation option to solve Reynolds-Averaged Navier–Stokes (RANS) equations. The coupled pressure-based solver was chosen with a second order implicit transient formulation for improved accuracy to solve low-speed incompressible flows. All the governing equations for the solution variables, which are decoupled from each other, are solved sequentially. With respect to the discretization of the convection terms in the transport equations for the velocity and the turbulence quantities, second-order upwind schemes are utilzed, since most of the flow can be assumed not to be in line with the mesh (Danao et al., 2014; Wekesa et al., 2014b, 2015, 2016; Wang et al., 2010). The green-gauss cell based method has been employed for calculating the gradients of the transport quantities on the faces of the cell boundaries. The under-relaxation factors are the CFD package solver settings default values which are sufficiently large enough imposed to avoid numerical instabilities in the solution.

The turbulent flow of the fluid is modelled by means of the Transition k–ω Shear Stress Transport (SST) turbulence model. The Transition k–ω SST turbulence model has shown a close prediction capability of Savonius rotor performance (Wekesa et al., 2014b, 2015; Tesch et al., 2015; Roy and Saha, 2013). The Transition SST model couples the k–ω SST with two other transport equations, one for the intermittency and one for the transition onset criteria, in terms of momentum thickness Reynolds number (Ansys Inc. Fluent 14.5 Documentation, 2015; Moshfeghi et al., 2012; Rocha et al., 2014). Further description regarding the resultant flow field and boundary conditions employed by the numerical wind tunnel technique required to achieve solutions using the Transition SST model has been reported by the authors in previous studies (Danao et al., 2014; Wekesa et al., 2014b, 2015, 2016).

The present simulations required an average of about 20 sub-iterations to make the solution converge at each physical time step. The time step convergence was monitored and the simulation was considered to have converged when residuals of all conserved variables fell below 1×10^{-5} (Wekesa et al., 2014b, 2015, 2016; Raciti Castelli et al., 2011). The calculations were performed on a computer having, Intel® Core™ i7-2600 CPU@3.40 GHz, 4 cores, 8 threads, physical RAM of 8 GB, and Windows 8 professional 64-bit operating system. Each simulation required a total Central Processing Unit (CPU) time of about 6 days.
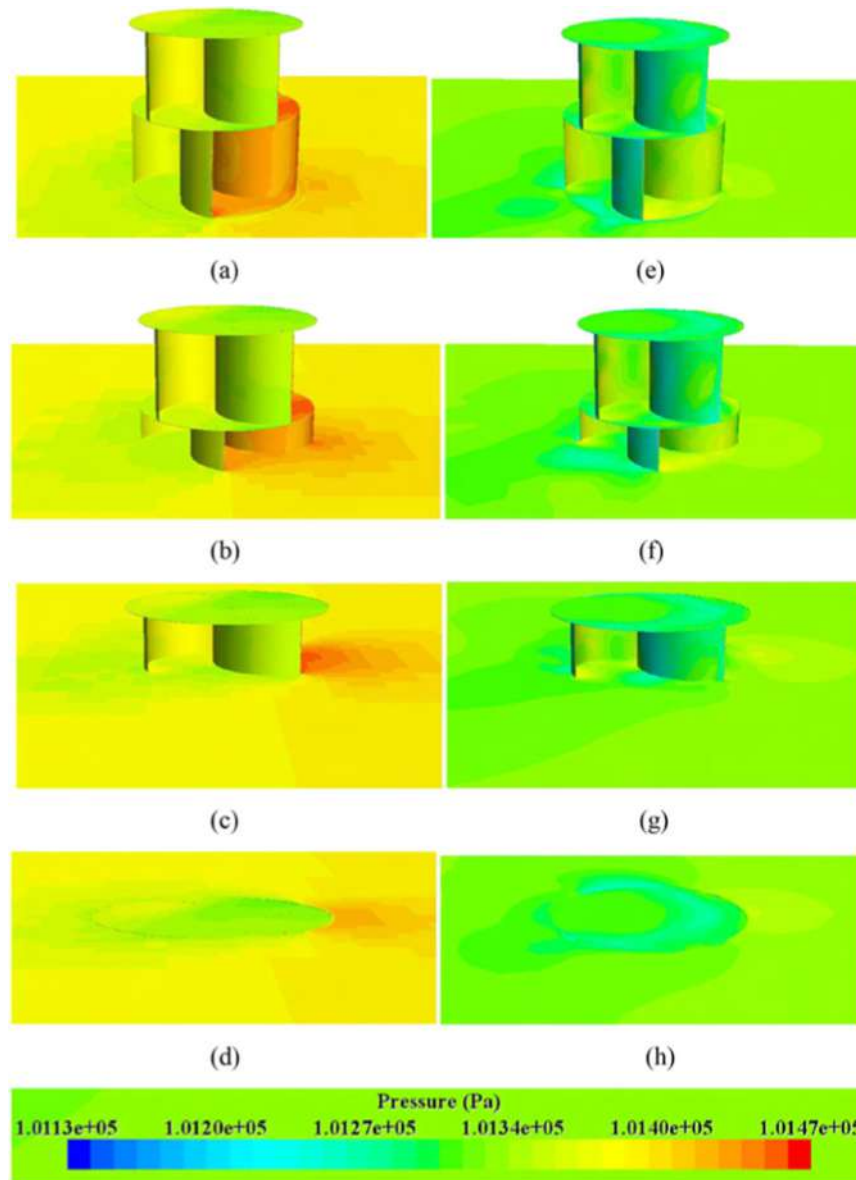
Fig. 15. Pressure contour plots along rotor at $\lambda=0.125$ (a–d) and $\lambda=1.5$ (e–h).

5.3. Predicted turbine performance

Fig. 14 shows predicted turbine's performance for both experimental and full three-dimensional CFD at free-stream velocity of 7 m/s for the turbulent flow case. The CFD simulations were run from $\lambda=0.125$ to $\lambda=1.50$ at intervals of 0.025 in order to provide a relative comparison to experimental measurements. The results presented in Fig. 14 demonstrates a satisfactory agreement in both the level and shape of the 3D predictions and the experiments. Observe from the figure that both torque and power coefficients are found to be very close to the experimental values, particularly, at higher tip-speed ratios ($\lambda > 0.4$). This could be attributable to the reduced changes in angle of attack between the relative velocity vector and the rotor following the drag differential between the advancing and retreating blades.

The average torque coefficient attains its highest value at low tip speed ratio and decays rapidly as the speed increases (Fig. 14 (a)). This implies that the present Savonius turbine (a two-stage rotor) has an excellent self-starting capability where high starting moment is generated on the turbine at rest. Due to the reduction of the relative velocity between the approaching wind and the

rotor, which results in lower moment due to induced drag forces, the moment starts to decay as soon as the turbine starts rotating.

From Fig. 14(a), the prediction looks in close proximity within the range for both experimental and CFD results. Observe in Fig. 14 (b) that C_P maximum peaks are nearly equal with values of 0.2050 and 0.2129 for experimental and numerical results, respectively.

5.4. Flow visualization

In order to explain the flow physics and associated self-starting capability by the two-stage Savonius rotor, the absolute pressure, velocity, and vorticity contours around the turbine rotor are plotted for the turbulent flow with $U=7$ m/s at tip speed ratios of $\lambda=0.125$ and 1.5 (Figs. 15–17). The absolute pressure was selected to provide a matching atmospheric boundary layer wind field observed in the experiment. As alluded to earlier in Section 2, measuring of the atmospheric boundary layer wind field was done in the wind tunnel using a simulated system made of multi-channel hot-wire anemometer, A/D board, PC machines and software components. The hot-film probe was calibrated beforehand in an empty wind tunnel.
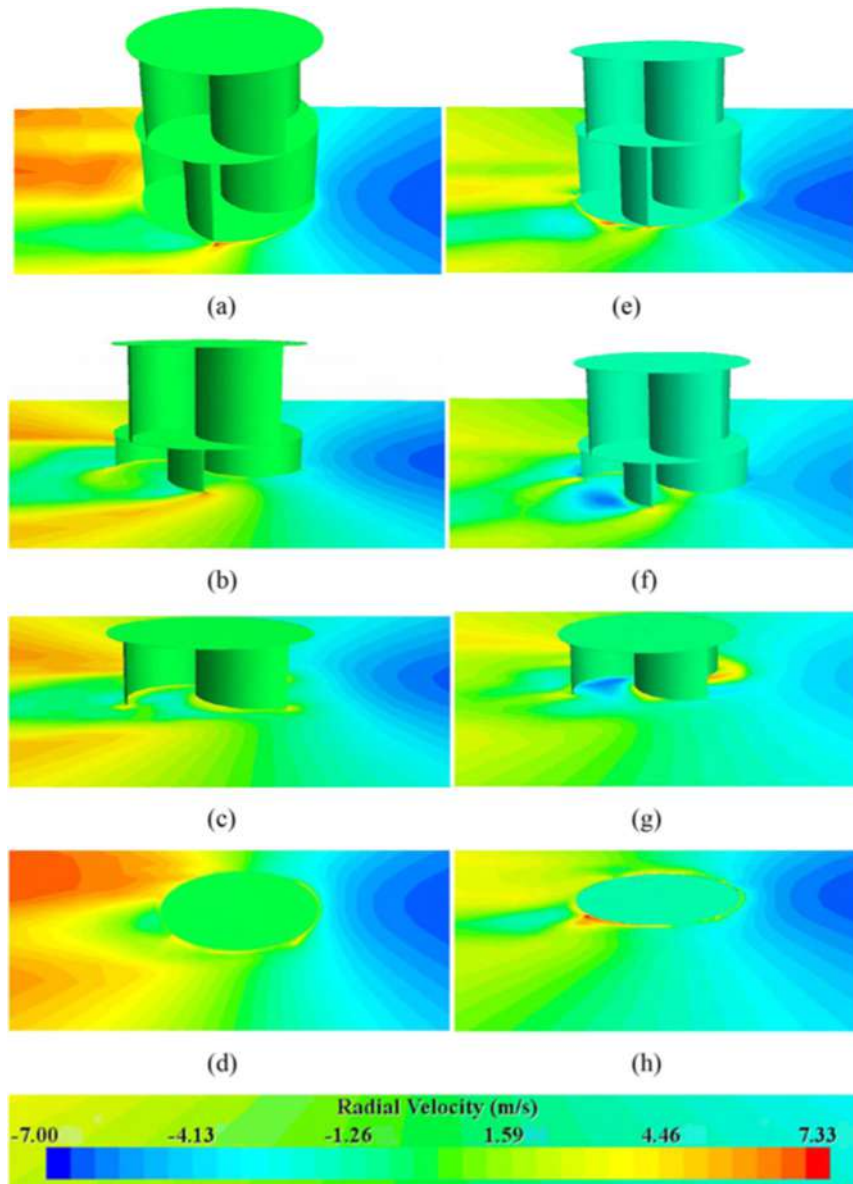
Fig. 16. Velocity contour plots along rotor at $\lambda=0.125$ (a–d) and $\lambda=1.5$ (e–h). (For interpretation of the references to color in this figure caption, the reader is referred to the web version of this paper.)

As can be seen in Fig. 15(a)–(d) at $\lambda=0.125$, the pressure contours show that advancing (convex) bucket suffers the highest pressure at the stagnation point in all the four positions along the rotor height. This can be attributed to the high relative velocity, which is nearly double the wind velocity.

Observe from the pressure contours in Fig. 15(e)–(h) that the pressure reduces significantly at $\lambda=1.5$. This pressure change behavior is associated with the rotor's deteriorating performance at $\lambda=1.5$ and elucidates the development of separation bubbles as can be seen in Fig. 17(e)–(h).

The velocity contours around the Savonius rotor for tip speed ratios at $\lambda=0.125$ and $\lambda=1.5$ for different positions along the rotor's height are as shown in Fig. 16. Fig. 16(a)–(d) shows that the convex face of the buckets experiences lowest velocities at stagnation point (blue regions); implying that the regions are subjected to separated flow with low velocities.

The reduced wind velocity near the rotor evidenced in Fig. 16 on the upstream results in a lower rotor moment which decays rapidly when the turbine starts to rotate as the speed increases. This justifies the improved self-starting capability by the rotor as reported early in the section. From Fig. 16(e)–(h), the stagnation point effect is also revealed with minimum value of torque coefficient as can be seen in Fig. 14(a) at $\lambda=1.5$.

Fig. 17 presents the distribution of vorticity around the turbine rotor. From the figure, vorticity is found to be near zero in the entire fluid domain except in the region around the rotor surfaces where flow separation and vortex shedding are the common phenomenon. This is a result of the unsteady working nature of the VAWT and continuous variation in the flow angle with respect to the rotor blades. The internal and external surfaces of the buckets are subjected to greatest vorticity values across the rotor with visible separation bubbles revealed more at tip speed ratio of $\lambda=1.5$ as can be seen in Fig. 17(e)–(h).

Therefore, the negative rotor performance at higher tip speed ratio (Fig. 14) is associated to the observed visible separation bubbles at $\lambda=1.5$ in Fig. 17. Generally, from Figs. 15–17, turbulent reduces the critical Reynolds number inducing early transition on the blade surface; this results in dynamic stall delay and flow separation deferment which significantly improves blade aerodynamic performance.
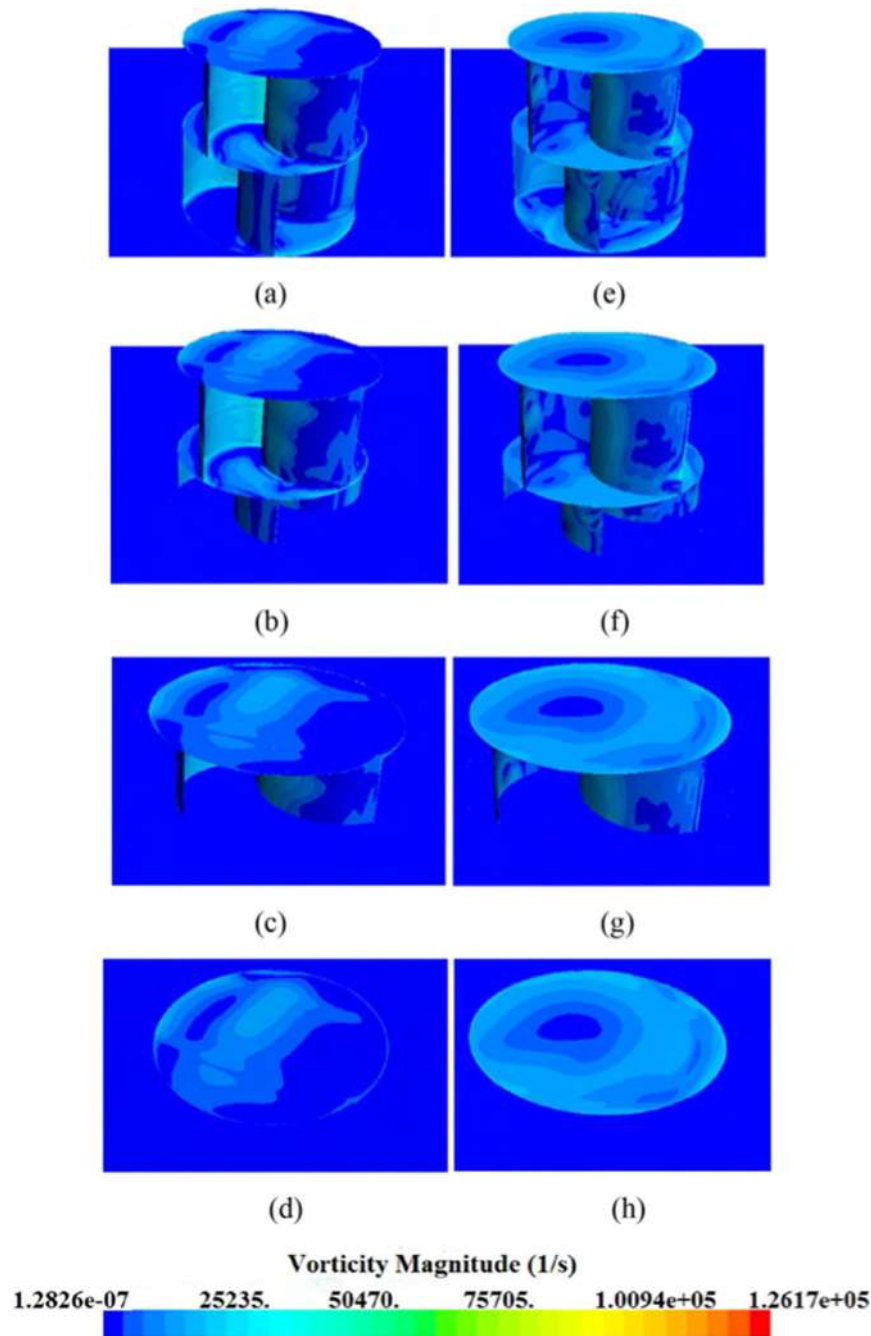
Fig. 17. Vorticity contour plots along rotor at $\lambda = 0.125$ (a–d) and $\lambda = 1.5$ (e–h).

6. Conclusion

Aerodynamic performance testing of a vertical axis wind turbine to investigate the influence of turbulence intensity was performed in a closed wind tunnel. A turbulent inflow was generated by elliptic wedge generators in the wind tunnel. The experimental tests were conducted on a double-stage Savonius rotor and the results are compared to the numerical data, which validated the numerical model. The study revealed that turbulent inflow impacted fluctuating aerodynamic loads on the turbine blade and, ultimately, its aerodynamic performance. Major findings emerging from the study may be summarized as follows:

- Experimental results showed that power production by wedge-generated turbulent flow was slightly higher than that produced by uniform flow, but a drastic reduction was evidenced at wind speeds above 7 m/s.

- Turbulence intensity had a dual influence on small wind turbines. The presence of a turbulent inflow increases the kinetic energy available to small wind turbines at low wind speeds; and also tends to decrease its efficiency at wind speeds near furling speed.

- The self-starting capability of the vertical axis wind turbine was improved on introducing an external turbulent inflow. This is attributable to reduction of the relative velocity between approaching wind and rotor at low tip speed ratios, which results in a lower moment that decays rapidly as the turbine starts rotating.

Although a turbulent inflow may increase turbine power

performance, care should be taken such that the blades must be designed to withstand the larger aerodynamic loads induced by turbulence. In addition, it is worth noting that the current study result implications are limited to small-scale wind turbines operating under turbulent flow conditions. However, the methodology developed in the analysis of aerodynamic performance of the small-scale turbine model, and the flow physics that causes the behavior may be transferable to larger scales for commercial wind rotor designers.

Acknowledgment

References

Ahmadi-Baloutaki, M., Carriveau, R., Ting, D.S.K., 2015. Performance of a vertical axis wind turbine in grid generated turbulence, Sustain. Energy Technol. Assess. 11, 178–185, http://dx.doi.org/10.1016/j.seta.2014.12.007.

Akwa, J.V., Vielmo, H.A., Petry, A.P., 2012. A review on the performance of Savonius wind turbines. Renew. Sustain. Energy Rev. 16, 3054–3064.

Ansys Inc. Fluent 14.5 Documentation, 2015.

Aslam Bhutta, M.M., Hayat, N., Farooq, A.U., Ali, Z., Jamil, S.R., Hussain, Z., 2012. Vertical axis wind turbine-a review of various configurations and design techniques. Renew. Sustain. Energy Rev. 16, 1926–1939.

Bertenyi, T., Wickins, C., McIntosh, S., 2010. Enhanced energy capture through gust-tracking in the urban wind environment. In: 48th AIAA Aerospace Sciences Meeting Including the New Horizons Forum and Aerospace Exposition, vol. 48. AIAA, Orlando, Florida, pp. 1–7, http://dx.doi.org/10.2514/6.2010-1376.

Bhuyan, S., Biswas, A., 2014. Investigations on self-starting and performance characteristics of simple h and hybrid h-Savonius vertical axis wind rotors. Energy Convers. Manag. 87, 859–867.

Cao, S., Tamura, Y., Kikuchi, N., Saito, M., Nakayama, I., Matsuzaki, Y., 2009. Wind characteristics of a strong typhoon. J. Wind Eng. Ind. Aerodyn. 97, 11–21.

Danao, L.A., Eboibi, O., Howell, R., 2013. An experimental investigation into the influence of unsteady wind on the performance of a vertical axis wind turbine. Appl. Energy 107, 403–411.

Danao, L.A., Edwards, J., Eboibi, O., Howell, R., 2014. A numerical investigation into the influence of unsteady wind on the performance and aerodynamics of a vertical axis wind turbine. Appl. Energy 116, 111–124.

Edwards, J.M., Danao, L.A., Howell, R.J., 2012. Novel experimental power curve determination and computational methods for the performance analysis of vertical axis wind turbines. J. Sol. Energy Eng. 134, 031008.

Emejeamara, F., Tomlin, A., Millward-Hopkins, J., 2015. Urban wind: characterisation of useful gust and energy capture. Renew. Energy 81, 162–172.

Fyrippis, I., Axaopoulos, P.J., Panayiotou, G., 2010. Wind energy potential assessment in Naxos Island, Greece. Appl. Energy 87, 577–586.

Gupta, R., Biswas, A., Sharma, K., 2008. Comparative study of a three-bucket Savonius rotor with a combined three-bucket Savonius three-bladed Darrieus rotor. Renew. Energy 33, 1961–1974.

He, Y., Chan, P., Li, Q., 2013. Wind characteristics over different terrains. J. Wind Eng. Ind. Aerodyn. 120, 51–69.

Howell, R., Qin, N., Edwards, J., Durrani, N., 2010. Wind tunnel and numerical study of a small vertical axis wind turbine. Renew. Energy 35, 412–422.

Islam, M., Ting, D.S.-K., Fartaj, A., 2008. Aerodynamic models for Darrieus-type straight-bladed vertical axis wind turbines. Renew. Sustain. Energy Rev. 12, 1087–1109.

Jeon, K.S., Jeong, J.I., Pan, J.-K., Ryu, K.-W., 2015. Effects of end plates with various shapes and sizes on helical performance wind turbines. Renew. Energy 79, 167–176.

Kooiman, S., Tullis, S., 2012. Response of a vertical axis wind turbine to time varying wind conditions found within the urban environment. Wind Eng. 34, 389–401.

Lubitz, W.D., 2014. Impact of ambient turbulence on performance of a small wind turbine. Renew. Energy 61, 69–73.

Mahmoud, N., El-Haroun, A., Wahba, E., Nasef, M., 2012. An experimental study on improvement of Savonius rotor performance. Alex. Eng. J. 51, 19–25.

Maldonado, V., Castillo, L., Thormann, A., Meneveau, C., 2015. The role of free stream turbulence with large integral scale on the aerodynamic performance of an experimental low Reynolds number s809 wind turbine blade. J. Wind Eng. Ind. Aerodyn. 142, 246–257.

McIntosh, S., Babinsky, H., Bertenyi, T., 2008. Unsteady power output of vertical axis wind turbines operating within a fluctuating free-stream. In: 46th AIAA Aerospace Sciences Meeting and Exhibit. Reno, Nevada.

Mcintosh, S., 2009. Wind Energy for the Built Environment. Department of Engineering, University of Cambridge, Cambridge, UK, pp. 105–106. https://www.repository.cam.ac.uk/handle/1810/252153.

Mikkelsen, K., 2013. Effect of Free Stream Turbulence on Wind Turbine Performance (M.Sc. thesis). Norwegian University of Science and Technology.

Moshfeghi, M., Song, Y.J., Xie, Y.H., 2012. Effects of near-wall grid spacing on SST-k–ω model using NREL phase VI horizontal axis wind turbine. J. Wind Eng. Ind. Aerodyn. 107–108, 94–105.

Mycek, P., Gaurier, B., Germain, G., Pinon, G., Rivoalen, E., 2014. Experimental study of the turbulence intensity effects on marine current turbines behaviour. Part I: one single turbine. Renew. Energy 66, 729–746.

Nasef, M., El-Askary, W., AbdEL-hamid, A., Gad, H., 2013. Evaluation of Savonius rotor performance: static and dynamic studies. J. Wind Eng. Ind. Aerodyn. 123, 1–11.

Pagnini, L.C., Burlando, M., Repetto, M.P., 2015. Experimental power curve of small-size wind turbines in turbulent urban environment. Appl. Energy 154, 112–121.

Paraschivoiu, I., 2002. Wind Turbine Design: With Emphasis on Darrieus Concept. Presses Inter Polytechnique, Polytechnic International Press, Canada. ISBN 2-553-00931-3.

Raciti Castelli, M., Englaro, A., Benini, E., 2011. The Darrieus wind turbine: proposal for a new performance prediction model based on CFD. Energy 36, 4919–4934.

Rocha, P.C., Rocha, H.B., Carneiro, F.M., Vieira da Silva, M., Bueno, A.V., 2014. k–ω SST (shear stress transport) turbulence model calibration: a case study on a small scale horizontal axis wind turbine. Energy 65, 412–418.

Rogers, A.L., Rogers, J.W., Manwell, J.F., 2005. Comparison of the performance of four measure-correlate-predict algorithms. J. Wind Eng. Ind. Aerodyn. 93, 243–264.

Roy, S., Saha, U.K., 2013. Review on the numerical investigations into the design and development of Savonius wind rotors. Renew. Sustain. Energy Rev. 24, 73–83.

Roy, S., Saha, U.K., 2015. Wind tunnel experiments of a newly developed two-bladed Savonius-style wind turbine. Appl. Energy 137, 117–125.

Saha, U., Rajkumar, M.J., 2006. On the performance analysis of Savonius rotor with twisted blades. Renew. Energy 31, 1768–1776.

Scheurich, F., 2011. Modelling the Aerodynamics of Vertical-Axis Wnd Turbines (Ph.D. thesis). University of Glasgow.

Seguro, J., Lambert, T., 2000. Modern estimation of the parameters of the Weibull wind speed distribution for wind energy analysis. J. Wind Eng. Ind. Aerodyn. 85, 75–84.

Sparks, P., Huang, Z., 2001. Gust factors and surface-to-gradient wind-speed ratios in tropical cyclones. J. Wind Eng. Ind. Aerodyn. 89, 1047–1058.

Sunderland, K., Woolmington, T., Blackledge, J., Conlon, M., 2015. Small wind turbines in turbulent (urban) environments: a consideration of normal and Weibull distributions for power prediction. J. Wind Eng. Ind. Aerodyn. 121, 70–81.

Tesch, K., Kludzinska, K., Doerffer, P., 2015. Investigation of the aerodynamics of an innovative vertical-axis wind turbine. Flow Turbul. Combust., pp. 1–16.

Torresi, M., Benedittis, F.A.D., Fortunato, B., Camporeale, S.M., 2014. Performance and flow field evaluation of a Savonius rotor tested in a wind tunnel. Energy Procedia 45, 207–216.

Turk, M., Emeis, S., 2010. The dependence of offshore turbulence intensity on wind speed. J. Wind Eng. Ind. Aerodyn. 466–471, 98.

Wang, S., Ingham, D.B., Ma, L., Pourkashanian, M., Tao, Z., 2010. Numerical investigations on dynamic stall of low Reynolds number flow around oscillating airfoils. Comput. Fluids 39, 1529–1541.

Wekesa, D.W., Wang, C., Wei, Y., Kamau, J.N., 2014a. Wind resource assessment and numerical simulation for wind turbine airfoils. In: 2014 15th International Workshop on Research and Education in Mechatronics (REM), vol. 15, IEEE, El Gouna, Egypt, pp. 1–9, http://dx.doi.org/10.1109/REM.2014.6920224.

Wekesa, D.W., Wang, C., Wei, Y., Danao, L.A.M., 2014b. Influence of operating conditions on unsteady wind performance of vertical axis wind turbines operating within a fluctuating free-stream: a numerical study. J. Wind Eng. Ind. Aerodyn. 135, 76–89.

Wekesa, D.W., Wang, C., Wei, Y., Kamau, J.N., Danao, L.A.M., 2015. A numerical analysis of unsteady inflow wind for site specific vertical axis wind turbine: a case study for marsabit and garissa in Kenya. Renew. Energy 76, 32–45.

Wekesa, D.W., Wang, C., Wei, Y., 2016. Empirical and numerical analysis of small wind turbine aerodynamic performance at a plateau terrain Kenya. Renew. Energy 90, 377–385.